Full elastic imaging – Shenzi Field, deep-water Gulf of Mexico

Allon Bartana[1], Jeff Codd[1] and David Kessler[1]*, Joakim Blanch[2], Drew Eddy[2], Ramses Meza[2], Varendra Rambaran[2] and J. P. Blangy[2] and Yi Huang [3] demonstrate the advantages of full elastic imaging using the OBN dataset acquired by Woodside Energy in 2019 to better image the sub-salt field.

Summary

Over the years Shenzi field in deep-water Gulf of Mexico became a test bed for evaluation of new seismic acquisition and processing technologies. These include 3D narrow azimuth streamer data, 3D-rich azimuth streamer data, and recently 3D OBN data (Mifflin et al, 2021). On the processing side, many types of processing techniques were used to image the various data types recorded over Shenzi field, from 3D ray-based Kirchhoff summation PSDM to Acoustic RTM PSDM and Acoustic FWI imaging. In the work presented here we demonstrate the advantages of Full Elastic imaging using the OBN dataset acquired by Woodside Energy in 2019 to better image the sub-salt field.

Introduction

In the past, computer capacity and cost led to the use of various approximations in the implementation of geophysical applications. These included use of ray-based velocity estimation (Stork 1992, Kosloff et al., 1996) and prestack depth migration (PSDM) algorithms (Gray et al., 2006), as well as the use of the acoustic assumptions as the basis for both velocity estimation and PSDM. With today's computing strength and cost, these limitations can be removed. In the last decade the industry has moved to wave equation applications for velocity estimation by means of full waveform inversion (FWI) (Tarantola 2005, Vigh et al., 2016) and two-way wave equation reverse time migration (RTM) (Baysal et al., 1983) as the leading method for application of PSDM. We can now progress further and move from using acoustic approximations to the use of full Elastic applications for both velocity estimation and PSDM.

Seismic imaging applications based on acoustic approximations have been in use for the past 40 years as an industry standard. This assumption considers the earth a fluid which supports propagation of P waves only and is justified on the basis that acoustic and elastic media produce the same travel times for pure P wave propagation. However, even for marine acquisition where only P waves are recorded, some of the reflected events propagate as S waves (through P-S mode conversions) along part of the propagation path in the subsurface. These shear waves supply important information about the subsurface geology and can help resolve subsurface rock properties as well as in-situ stress. In addition, anisotropy is only approximated with acoustic imaging, a fact which causes artifacts from slowly propagating quasi-shear waves. Today we are able to use the full elastic wave equation as the basis for PSDM and velocity estimation in an economic way. This is done without any approximations, enabling the use of both P and S waves in imaging (i.e., the full wavefield).

Another recent industry change in the application of depth imaging is to introduce FWI imaging (FWII), wherein the final image is directly constructed from the velocity model by calculation of reflectivity (Mifflin et al., 2021). The prevailing industry direction is to use FWI imaging resulting from the use of full Elastic implementation of FWI. Another option, which we advocate for here, is to use the full Elastic wave equation as the basis for implementation of PSDM. Using RTM as the underlying algorithm, this results in Elastic reverse time migration (ERTM).

In this work we present the application of ERTM using a proprietary OBN survey recorded over the Shenzi field in deep-water Gulf of Mexico. Over the years, many geophysical applications and various acquisition setups were used to better image the Shenzi field (Howard 2007, Mifflin et al., 2021). This includes narrow azimuth, rich azimuth and OBN acquisitions as well as Acoustic RTM PSDM (ARTM) and Acoustic FWI imaging (FWII). Application of ERTM using Shenzi OBN data can now be evaluated and compared to acoustic-based imaging (both ARTM and FWII) performed using the same OBN data over the field.

Elastic RTM

Until recently, most seismic data processing has been carried out under the acoustic assumption. Accordingly, the layers of the earth are considered as fluids without resistance to shear tractions. Although obviously this description does not represent the earth's response properly, it correctly predicts the arrival time of the primary P waves and gives an estimate of the amplitude decay due to geometrical spreading. Consequently, despite using the 'wrong' physics, seismic data imaging based on acoustic approximation has been very successful.

A physical model which better matches the response of the earth is an anisotropic anelastic (or visco-elastic) solid material

[1] SeismicCity | [2] Woodside Energy | [3] TGS
* Corresponding author, E-mail: dkessler@seismiccity.com
DOI: 10.3997/1365-2397.fb2024023

(Samec and Blangy, 1992). The model correctly predicts the generation of shear waves in addition to the P waves, and accounts for the attenuation as well as the phase distortion of waves during propagation. Operating under the elastic assumption enables us to extract more useful information from the seismic data. The amplitudes of the reflected arrivals are closer to the amplitudes of real data and therefore can be used to improve FWI applications and generate better data for AVO analysis.

The shear waves and converted waves arrivals which seldom have been used in seismic imaging contain additional information on the subsurface material properties. In addition to the currently used P wave imaging, imaging can be carried out using pure shear arrivals or converted wave arrivals. Using ERTM, three types of waves are present, namely qP waves, qSv and qSh waves' which usually travel in different paths (Aki and Richards, 1980, Ben-Menahem and Singh, 1981). In marine environments the source is P, so most of the converted waves are qSv. As the subsurface is illuminated by both qP and qSv waves, in areas of poor illumination by one type of wave, there may be compensation by good illumination from the other type. In addition, shear waves travel with a velocity which is different from that of P wave velocity, and thus determining S wave velocity helps resolve subsurface material properties. Furthermore, Shear waves in general are more sensitive to anisotropy, and a combined use of P and S waves enables tightening of the resolution of anisotropic parameters.

When a propagating P wave encounters a material interface, it creates four new waves, namely reflected and transmitted P waves and reflected and transmitted converted S waves (see Figure 10, Langton et al., 2019). Similarly, a propagating S wave will create transmitted and reflected S waves and reflected and transmitted converted P waves. The degree of conversion depends on the layer interface and angle of incidence. An interface across which the velocity changes abruptly will create a high degree of conversion. Conversely, an interface across which the velocity change is spread more diffusely over an area will create converted waves. Converted waves are present in all reflected seismic data but seldom used to their full potential in seismic imaging. In marine streamer acquisition the wave originating from the source and the reflected waves recorded by the hydrophones are both P waves, since shear waves do not propagate in a fluid. However, many mode conversions occur in the subsurface, and part of these conversions will be recorded as P waves at the surface. In marine OBN acquisition both P and S waves are recorded by the hydrophones and geophones of the nodes. In the case here we used as input the P-Z summed data (Pacal et al., 2015). Using ERTM however, the horizontal components which contain mainly S waves can be used as well.

Elastic RTM migration is based on the same principle as acoustic RTM except that three displacement components are propagated instead of the pressure field. Unlike conventional RTM there are several options to create migrated images. Extracting P and S wave amplitudes from the displacement components, PP, PS, SS, and SP images can be created (Duan and Sava, 2010).

The advantages of elastic imaging were demonstrated for both Gulf of Mexico marine salt environment (Jing et al., 2017) as well as onshore US Permian basin (Langton et al., 2019). This can be extended to many other geological settings, both using marine and land seismic data. Converted shear waves are normally slower than the compressional waves and will appear on migrated PSDM gathers as 'slow events' that are commonly mistaken for multiples. Use of elastic PSDM enables us to correctly migrate both the faster propagating P waves as well as the slower propagating S waves. Use of both the P and S waves will result in a more detailed PSDM image as well as increased resolution of the migrated PSDM data.

The ERTM algorithm is based on direct solution of the equations of dynamic elasticity. The equation of conservation of linear momentum:

$$\rho \ddot{u}_i = \frac{\partial \sigma_{ji}}{\partial x_j} + f_i \tag{1}$$

where ρ is density, $\ddot{u}_i$ is the second time derivative of the displacement component and $i = 1,2,3$. σ_{ij} represents the 6 stress components. The stresses are related to the strains through Hook's law:

$$\sigma_{ij} = c_{ijkl} e_{kl} \tag{2}$$

where e_{kl} are the strains and c_{ijkl} are the 81 elastic coefficients, of which 21 are independent. With 21 elastic coefficients any type of anisotropy can be modelled. The stress-displacement relation reads:

$$e_{ij} = \frac{1}{2}\left(\frac{\partial u_i}{\partial x_j} + \frac{\partial u_j}{\partial x_i} \right) \tag{3}$$

(Aki and Richards, 1980, Ben-Menahem and Singh, 1981). Although the advantage of fully elastic data processing is

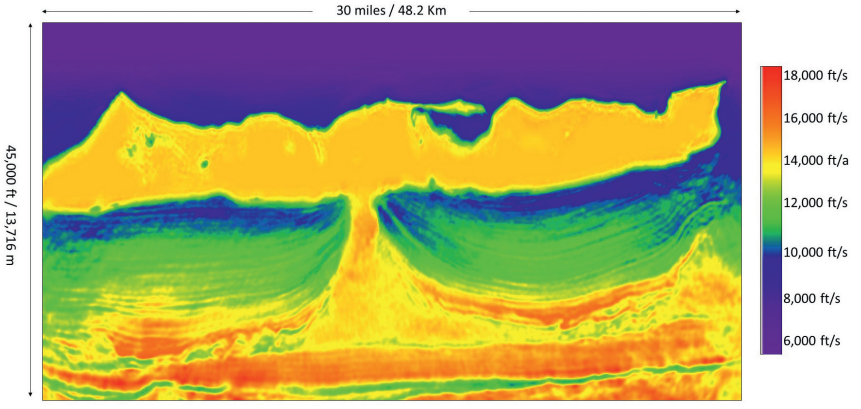

Figure 1 P wave velocity model used as the basis for construction of the S wave velocity and density models.

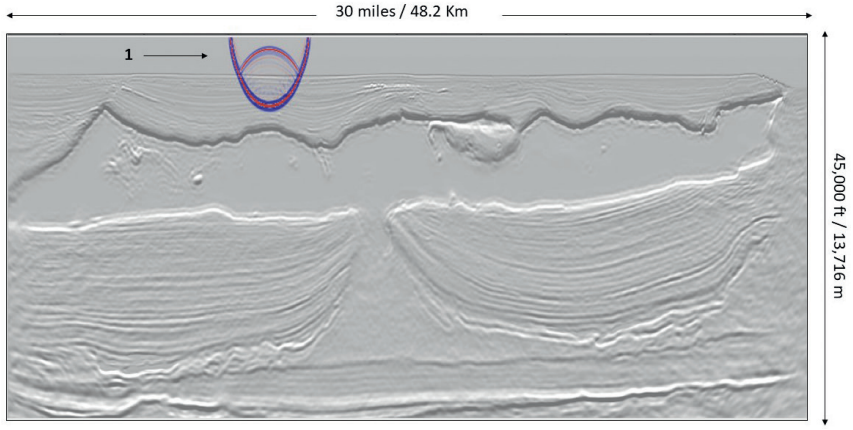

Figure 2 P wavefield at 1.5 seconds of propagation. The arrow marked 1 points to the P wave direct arrival.

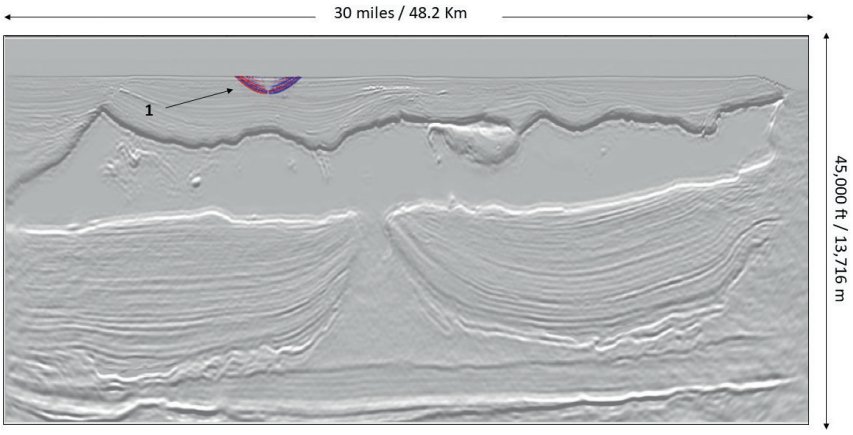

Figure 3 S wavefield at 1.5 seconds of propagation. The arrow marked 1 points to the P to S conversion occurring at the sea floor.

obvious, there are challenges in its implementation. Elastic forward modelling and ERTM are based on the numerical solution of the equation of dynamic elasticity. There are practical difficulties in implementing elastic solution schemes. A large number of spatial variables are required (three displacements, three particle velocities, three accelerations, 6 stress components, 21 elastic constants, and density). However, using optimised numerical schemes (Bartana et al., 2015) both algorithmic and optimisation challenges can be solved, enabling the routine use of ERTM in production environment.

To apply ERTM PSDM, we need to invoke an Elastic model. This requires the addition of the Elastic S velocity along the axis of symmetry, density, and Thomsen's anisotropy parameter gamma to the parameterisation of the Acoustic model used for ARTM (P velocity along the axis of symmetry, Thomsen's anisotropic parameters delta and epsilon, as well as dip and azimuth). The density field is related to changes in amplitude only. The S velocity field determines the speed that the converted waves are travelling and therefore affecting the overall wave propagation time. In the work presented here we used a TTI anisotropic Elastic model. This was constructed by use of an Acoustic TTI model previously constructed for application of Acoustic imaging as the base model. Well data were used for calculation of the S velocity and empirical formulas for construction of the density model (Figure 1).

For the calculation of the S velocity model, logs from 40 wells were used. The P velocity from the acoustic model was extracted at the well locations and used for calculation of S velocity using various empirical relations. The resulting S velocity functions were then compared to the S velocity logs. The Castagna formulation (Castagna et al., 1985), as fitted to the Shale formation, resulted in a very good match between the calculated S velocity and the well logs, so it was used to create the S velocity model. For calculation of the density field, Gardner's equation was used (Gardner et al., 1974). The resulting Elastic model consisted of P velocity ranging between 4859 ft/s to 18,871 ft/s, S velocity ranging between zero (in the water column) and 11,608 ft/s, and density field ranging between 1.0 g/cm3 and 2.696 g/cm^3. The density in the salt body was about 2.5 g/cm^3.

Elastic wave propagation in the Shenzi field area

In the case of marine seismic data acquisition, the source located in the water layer generates a P wave front. Converted waves are generated at the sea floor (the transition from water to the solid earth). In a streamer survey, the receivers are located in the water layer and will record P waves arrivals only. In an OBN survey, the nodes are located at the water bottom and will record both P waves and S waves. The hydrophone and the vertical component records P waves, and the S waves are recorded mainly by the horizontal components. In both of the streamer and OBN cases, mode-converted wavefronts are generated in the sub-surface. Even though the recorded wavefield consists of P waves, some of the down-going and up-going waves are at least partially propagating as S waves. ERTM calculates any possible wave path including all of the mode conversions.

To analyse the amount of mode converted data in the Shenzi field area, we review wave propagation snapshots generated using the Elastic model applied for the ERTM. The P and S

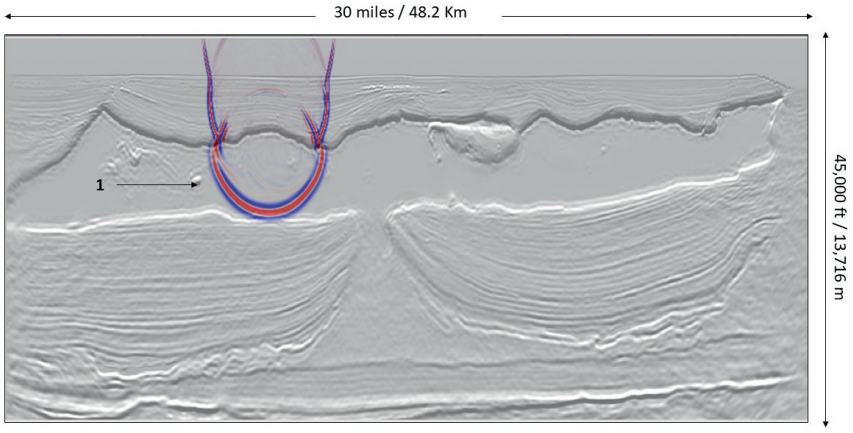

Figure 4 P wavefield at 2.5 seconds of propagation. Arrow 1 points to the P wave direct arrival traveling with faster salt velocity inside the salt body.

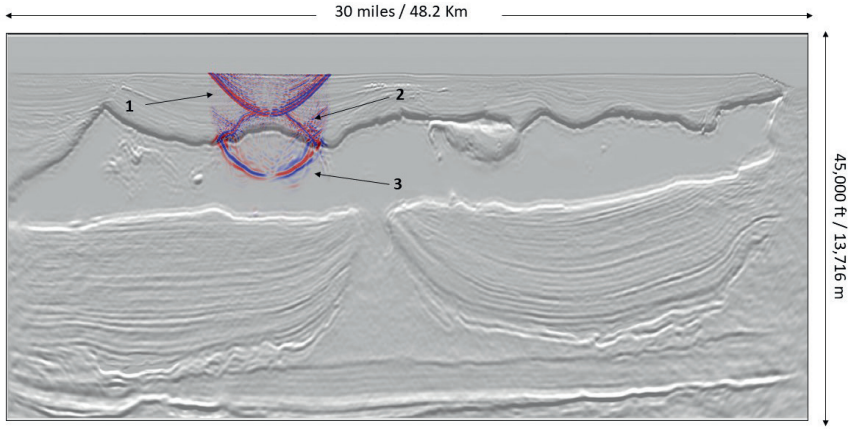

Figure 5 S wavefield at 2.5 seconds of propagation. Arrow 1 shows the P to S conversion direct wave generated at the sea floor. Arrow 2 shows the P to S conversion generated at the top salt. Arrow 3 shows the P to S conversion at the top salt. This S wave front is travelling in the salt with the salt S velocity.

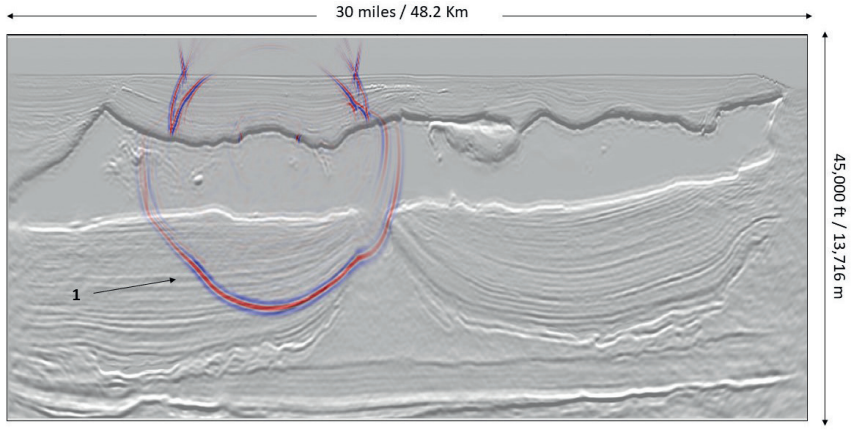

Figure 6 P wavefield at 3.5 seconds of propagation. Arrow 1 marks the direct P wave front propagating below the salt body.

wave propagation snapshots are shown in Figures 2-9. Using a P source located at the surface, Figures 2 and 3 show the P and S wavefields after 1.5 seconds of propagation. The P wavefield display shows that only a P wave is propagating in the water layer and a P wave is reflecting from the water bottom interface. The S wave display shows that a converted S wave is generated at the water bottom resulting from the P wavefront that is impeding on the interface between water and the solid earth. Figures 4 and 5 show the P and S wavefields at 2.5 seconds of propagation. The P wavefield display shows the P wave front reaching the top salt and starting to propagate with the faster salt velocity. The P wave reflected upward from the top salt is shown as well. The S wavefield display shows three main wavefronts: (i) the slower downward propagating S wavefront that was generated at the water bottom, (ii) the S wavefront that is generated at the sediment to salt interface from the downward propagating P wave and (iii) the upward propagating reflected S wave, generated at the top salt interface. At this propagation time, the S wavefronts are detected inside the salt body as well as in the sedimentary section between the top salt and water bottom. Figures 6 and 7 show the P and S wavefields at 3.5 seconds of propagation. The P wave display shows the P wavefront emerging from the salt body and reaching the producing field around the salt stalk. The S wave display shows a series of P-S converted waves generated at the base of salt interface as well as complex path P-S head waves connecting the P wave propagating at the water layer to the S waves propagating inside the salt body. Careful analysis of the wavefronts shown in Figure 7 reveals several S wavefronts that are propagating in a direction perpendicular to the dips of the reservoir sands around the salt stalk. These downward propagating

S waves will trigger both P and S waves reflecting back from the sub-salt layers that are the reservoir sand layers. Figures 8 and 9 show the P and S wavefields at 4.5 seconds of propagation. The P wave display shows the downward propagating P wavefronts propagating along the deeper salt body and the sub-salt sedimentary section. The S wave display shows additional downward propagating S wavefronts propagating inside the tabular salt body as well as the salt diapir and at the sub-salt sedimentary section. Analysis of the wavefronts shown in Figure 9 shows the large amount of converted wave energy that is propagating in the sub-salt section. The wavefield recorded by the ocean bottom nodes consists of both P waves (hydrophone) and S waves (horizontal components). Both can be used as input to ERTM. In the work here we used only the P wavefield and vertical components as input after P-Z summation. The ERTM results are shown in the next section. In the results shown, waves converted in the sub-salt section and recorded as P waves can be used to improve the imaging of the sub-salt section by means of ERTM.

Elastic imaging results

Using the Shenzi pre-processed OBN dataset and the TTI anisotropic Elastic model, ERTM was applied. Using reciprocity, 3576 common receiver gathers were migrated. Post migration, the migrated shots were stacked to produce the imaged PSDM stack volume. For analysis of the results, we compare the ERTM stack to two stacked images produced using the Acoustic wave equation. The first comparison is with ARTM. In this comparison we compare the raw ERTM stack to the raw ARTM stack. The application of ERTM was done using maximum frequency of 20 Hz and is compared to

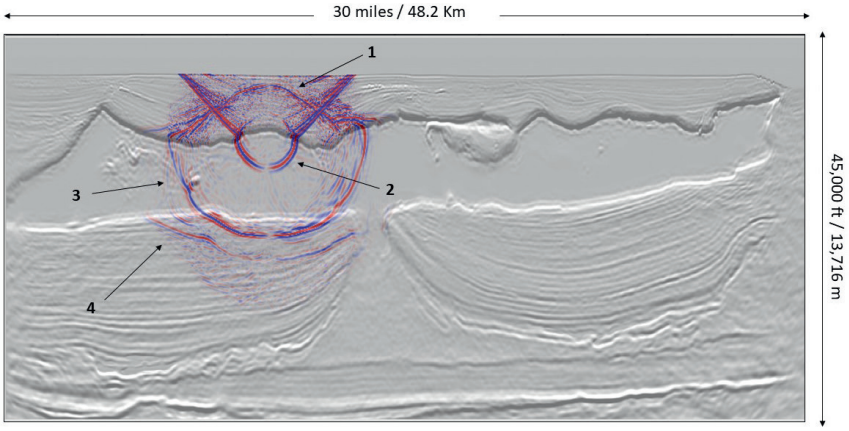

Figure 7 S wavefield at 3.5 seconds of propagation. Arrow 1 shows the P to S conversion occurring at the top salt. Arrow 2 is a complex P to S conversion of the head wave travelling above the salt. Arrow 3 is the P to S conversion at the top salt. Arrow 4 is P to S conversion at the base of salt. This wavefront will travel in the subsalt section before the 'direct' P to converted wave occurring at the top salt.

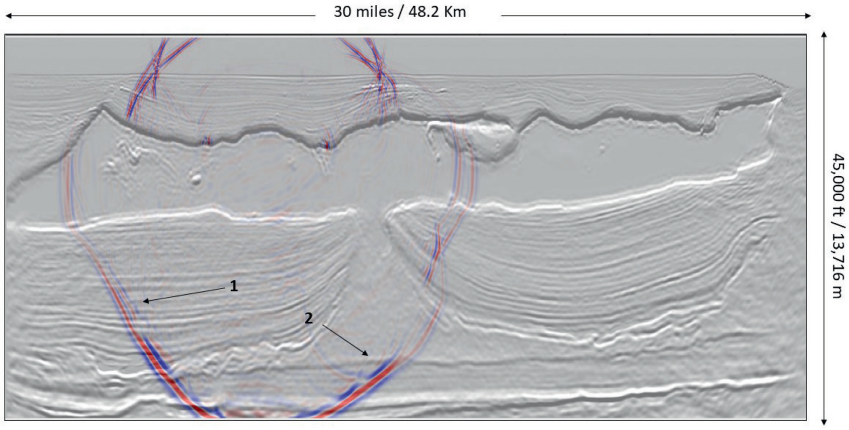

Figure 8 P wavefield at 4.5 seconds of propagation. Arrows 1 and 2 point to the direct P wave. Arrow 1 is the direct P wave front traveling in the sub-salt sedimentary section. Arrow 2 is the direct P wave front travelling in the deeper salt body.

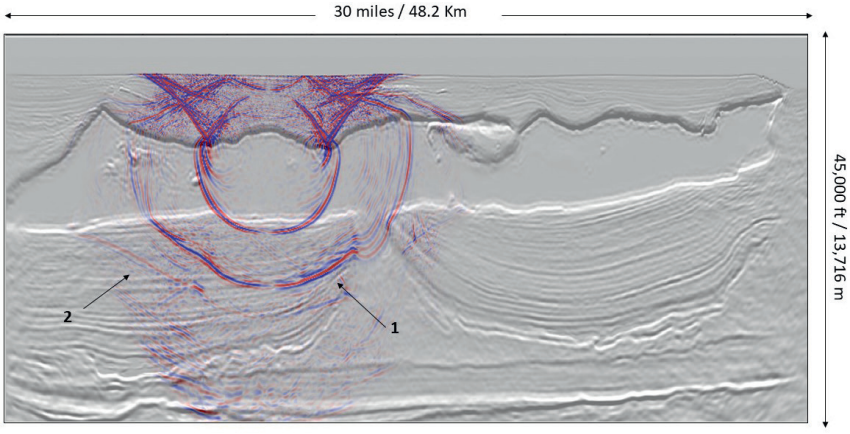

Figure 9 S wavefield at 4.5 seconds of propagation. Arrow 1 is the 'direct arrival' P to S conversion at the top salt. The wavefront will reflect back from the sub-salt sands that are part of Shenzi field. Arrow 2 is S wavefront converted from the P wavefront to S.

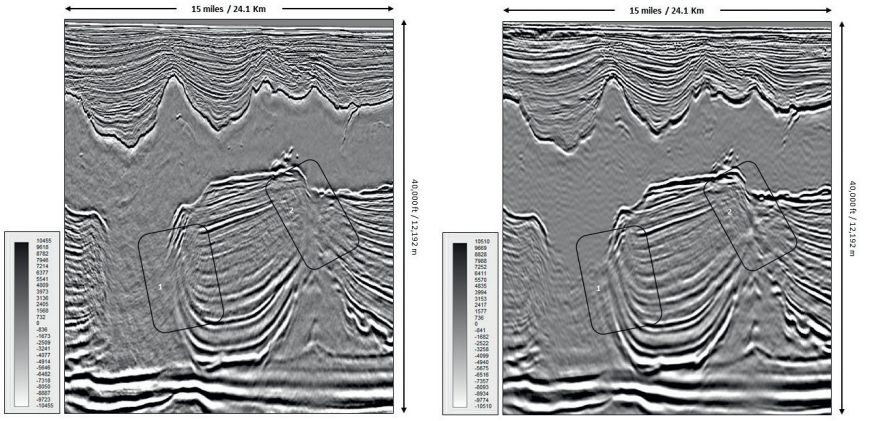

Figure 10 Left: 30 Hz Raw Acoustic RTM PSDM. Right: 20 Hz Raw Elastic RTM PSDM. Vertical exaggeration (V.E.) is 1:2.6. The annotation marked by 1 and 2 show areas of difference. In the area marked by 1, the ERTM includes sub-salt steep dip events that are not imaged by ARTM. In the area marked by 2, the ERTM provides a more complete image showing sub-salt faults separating two different geological units with different dips. The ARTM image in this area is lacking these details.

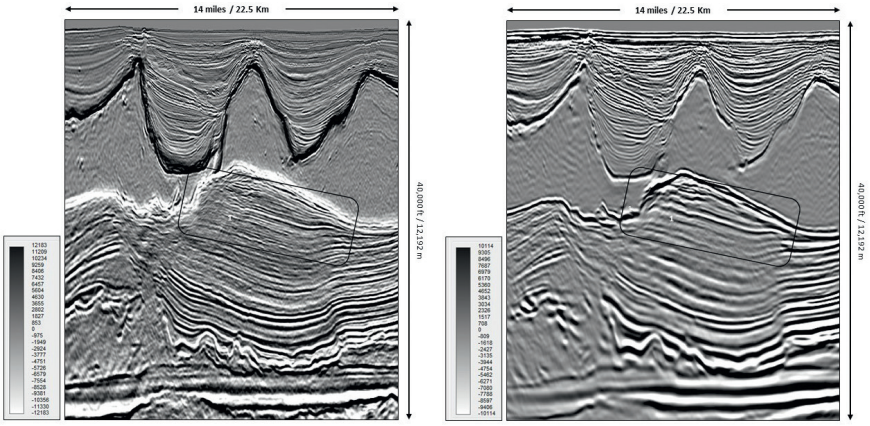

Figure 11 Left: Acoustic FWI imaging. Right: 20 Hz Elastic RTM with post processing applied. V.E. is 1:2.25. The sub-salt event marked by 1 is imaged by the ERTM compared to a 'no illumination' area shown in the FWI image.

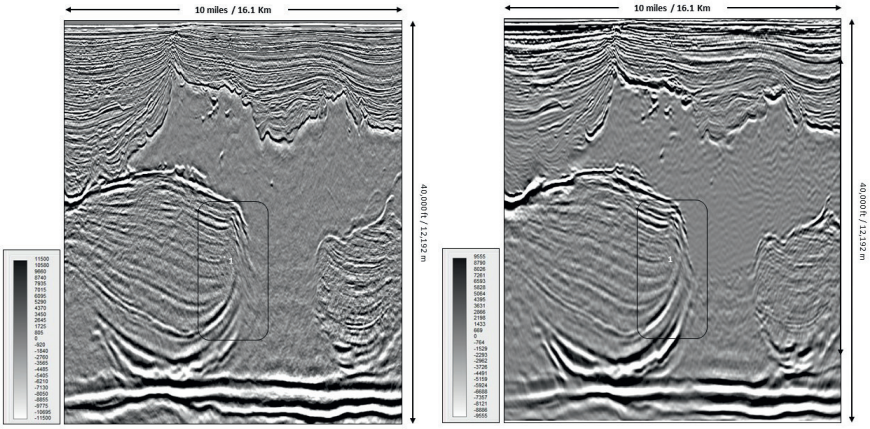

Figure 12 Left: 30 Hz Raw Acoustic RTM. Right: 30 Hz Raw Elastic RTM. V.E. is 1:2.25. The steep dip sub-salt event marked by 1 is well imaged by the ERTM compared to a 'no illumination' area in the ARTM image.

previously done 30 Hz ARTM. Figure 10 shows ARTM and ERTM imaging beneath salt. Eocene and Cretaceous age formations are marked by 1 and Upper Miocene age events are marked by 2.

The Shenzi OBN dataset was also imaged using full waveform inversion imaging (FWII). In the past few years, FWII has been added as a tool to create a migrated image directly from the resulting velocity model. In most cases this is done using Acoustic FWI application. As an FWI image consists of calculation of reflectivity directly from the velocity model, an image with less noise can be generated. However, if the inversion procedure does not include a full Elastic formulation, the image will lack contributions from both P waves and S waves. This is demonstrated in the data comparisons below. Since post processing was added to generate the FWII stack, we applied noise reduction filtering to the raw ERTM stack volume before comparing to the FWII volume. In the next sections we compare the Elastic imaging results to Acoustic imaging by reviewing of key geological features that are important to well placement.

Sub-salt imaging

For many sub-salt exploration targets, the processing objective is to image the edge of the trap, which for Shenzi is the truncation of the sedimentary section against the salt flank. Using various Acoustic imaging techniques and various types of seismic data (i.e., Streamer and OBN), this task is known to be difficult. The reason is that in many cases the P wave reflections travelling upwards reach the salt flank past the critical angle and therefore do not reflect off this interface, are not transmitted to the surface or ocean bottom receivers, and therefore fail to

image the area in close proximity to the salt flank. However, in many cases seismic mode conversion occurs when the P waves reaching the salt body are converted to S waves that propagate upwards inside the salt body. These S waves will then convert back to P waves at the top of salt and will be recorded at the surface as P waves. Using ERTM, these waves are included in the constructed image as mode converted wave propagation is included in the migration process. The result is clearer imaging of the truncation of the sub-salt sedimentary section events against the salt flank. Three imaging examples demonstrating the ability of ERTM to image the up-dip section of sub-salt events are shown. Figure 11 shows imaging of a series of low dip sub-salt events between base of salt and Middle Miocene. Figure 12 shows imaging of a steep dip event truncating against the salt body. These are Middle and Lower Miocene age formations. Figure 13 shows imaging of steep dip events in both sides of a sub-salt basin. The events marked by 1 are Oligocene, Eocene and Cretaceous age formations. The events marked by 2 are Lower Miocene age formations.

Imaging of sub-salt faults and unconformities

A common deficiency of PSDM imaging is the ability to image faults, in deeper basins or below salt. This can result in erroneous interpretation and oversimplified maps of sub-salt structures. When using ERTM however, the full recorded wavefield is accounted for during imaging (i.e. utilising all P waves and S waves and their mode conversions). This allows for additional details to be imaged in the sub-salt section. This is demonstrated

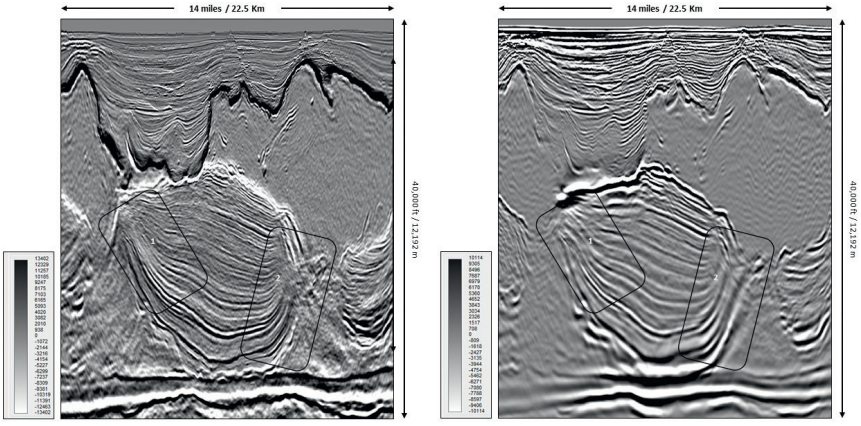

Figure 13 Left: Acoustic FWI imaging. Right: 20 Hz Elastic RTM with limited post processing applied. V.E. is 1:2.3. Steep dip sub-salt events marked by 1 and 2 are well imaged by ERTM.

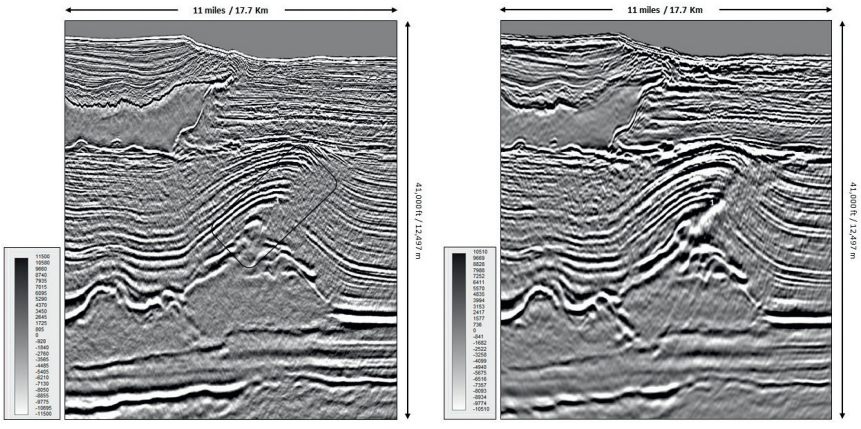

Figure 14 Left: 30 Hz Raw Acoustic RTM. Right: 20 Hz Raw Elastic RTM. V.E. is 1:1.6. The area marked by 1 shows a major thrust cutting the structure, just East of the crest.

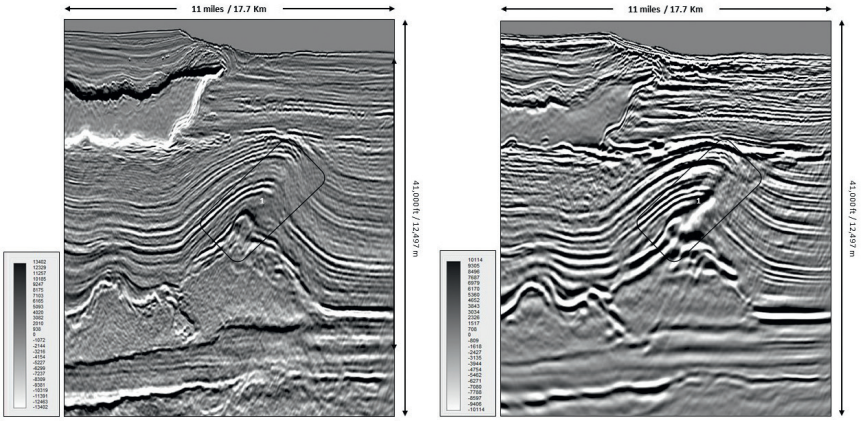

Figure 15 Left: Acoustic FWI imaging. Right: 20 Hz Elastic RTM with post processing applied. V.E. is 1:1.6. The FWI image does not include the thrust fault, which is clearly imaged using ERTM.

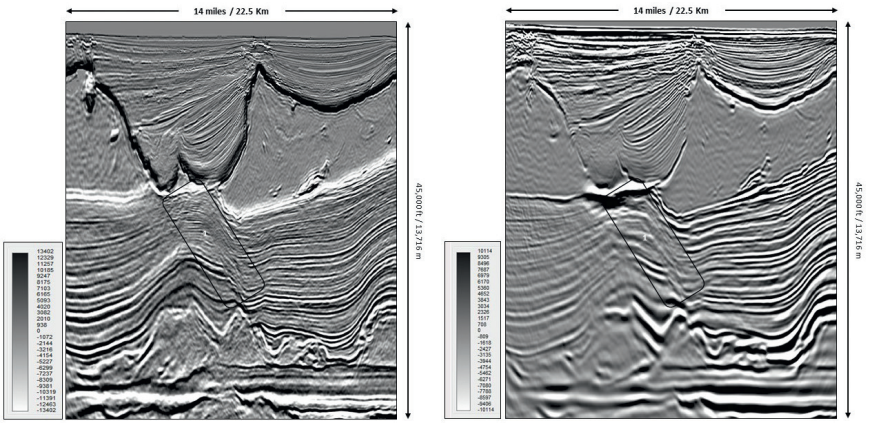

Figure 16 Left: Acoustic FWI imaging. Right: 20 Hz Elastic RTM with post processing applied. V.E. is 1:2.0. The sub-salt fault zone marked with the letter 1 is imaged using the ERTM, while the FWI image includes a 'poor illumination' zone.

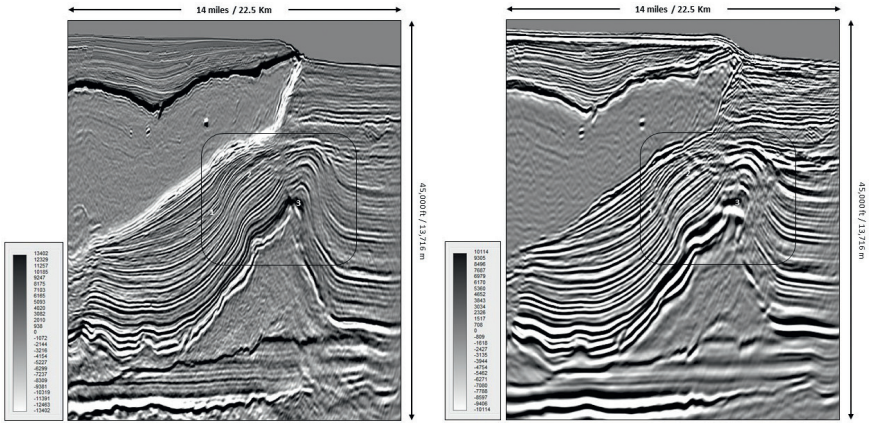

Figure 17 Left: Acoustic FWI imaging. Right: 20 Hz Elastic RTM with post processing applied. V.E. is 1:2.0. Sub-salt faults imaged by ERTM are marked by 1, 2 and 3. Fault 1 is imaged by the ERTM but not by the Acoustic FWII. Fault 2 is imaged by FWI in the deeper part and better by the ERTM in the shallower part. Fault 3 is imaged by the ERTM but not by the Acoustic FWII.

in the two sections shown in Figures 14 and 15 where clear faults are imaged by ERTM in Middle Miocene, Oligocene, Eocene and Cretaceous formations.

The seismic image of Figure 14 displays a prominent anti-cline near the Shenzi field. The ARTM image includes a poorly imaged area marked with the number 1. A potential variation on the interpretation of this section could be one continuous (un-faulted) anticlinal structure, with a very steep, nearly vertical Easterly limb. However, on the ERTM image, a major thrust fault is clearly imaged, with a better focused salt core below, and what could be interpreted as a fault plane reflection. Furthermore, the interpretation of the ERTM section indicates that the stratigraphy is likely to be offset across the fault.

FWI imaging in this area is examined as well (Figure 15). As the FWI image results from a velocity model, it actually provides a simplistic representation of the geology. Examination of the FWI image from ARTM shown in Figure 15 suggests a continuous structure with a very steep eastern limb. Interpretation of this image will result in a simplistic interpretation of the geology. On the other hand, the ERTM image includes the thrust fault (marked by 1), and the interpretation of this image will result in a faulted trap.

The area shown in Figure 16 includes an unconformity in the sub-salt section. The events marked by the black box are from Upper Miocene to Cretaceous age formations. The FWI image (on the left) shows a typical 'illumination hole' common in imaging done using Acoustic approximations. The ERTM image (on the right) includes a clear image of the main faults (marked by 1) separating the two geological units with very different local dips. The reflection from the sub-salt faults was propagating in the salt as converted wave and therefore can be imaged using ERTM.

The area shown in Figure 17 includes a compartmentalised thrusted structure. The events marked by the black box are from Upper Miocene to Cretaceous age formations. The FWI image produced by the Acoustic wave equation suggests a continuous structure. The ERTM image shows on the other hand, several faults cutting the structure. Once again, imaging of geological details that are part of deeper section or sub-salt structures will lead to a more correct interpretation of the sub-salt structure and will result in a better field development plan, with wells placed to target the various compartments of the sub-salt structure.

Summary

Every decade has seen a step change in industrial application of PSDM algorithms for seismic imaging of complex areas. In the 1990s ray-based 3D Kirchhoff summation algorithms became the main application used by the industry. In the 2000s, wave equation-based algorithms became operational, based on the solution of the one-way wave equation. In the 2010s, reverse time migration took over as the leading PSDM application. Based on the solution of the two-way wave equation, RTM enabled reliable imaging of complex geological structures. However, most of the industrial RTM applications are based on the solution of the Acoustic wave equation, which is a fundamental approximation of the full Elastic wave equation. With the availability of stronger computational platforms, we can today move a step forward with the full Elastic implementation of the wave equation. The term

'full' means that the equation of dynamic elasticity are directly used, without the need to include any approximations or short cuts.

In the work shown here, ERTM was tested using OBN data recorded over the Shenzi field area in deep-water Gulf of Mexico. Examination of the results shows that seismic imaging can be improved in places by moving from Acoustic approximations to use PSDM based on the full Elastic wave equation. Different depth imaging methods have their strengths and weaknesses ranging from computational cost and ability to resolve different features of the subsurface. Using the full Elastic wave equation, the entire wavefield is used to construct the migrated image. We compared here ERTM to ARTM as well as ERTM to Acoustic FWI imaging done using acoustic approximations. ERTM has been shown to be able to image geological features that the other methods do not, as well as other methods showing a few features not imaged by the ERTM. This suggests that a combination of depth imaging methods can lead to optimal depth imaging.

We foresee the industry moving to develop and use FWI algorithms based on the solution of the full Elastic wave equation for both velocity estimation and imaging. Having Elastic FWI will enable us to construct the S wave velocity directly from the seismic data. In the area of depth imaging we demonstrated that ERTM PSDM is a depth imaging tool that should be part of a depth imaging applications set used in commercial projects.

Acknowledgments

We thank Woodside Energy for its collaboration in the construction of the Elastic model and application of ERTM. We thank Woodside Energy and Repsol for the permission to publish this work.

References

Aki, K. and Richards, P.G. [1980]. *Quantitative Seismology: Theory and Methods*. WH Freeman and Co.

Bartana, A., Kosloff, D., Warnell, B., Connor, C., Codd, J., Kessler, D., Micikevicius, P., Mckercher, T., Wang, P. and Holzhaur, P. [2015]. *GPU implementation of minimal dispersion recursive operators for revrese time migration*. SEG annual meeting.

Baysal, E., Kosloff, D. and Sherwood, J. [1983]. Reverse Time Migration. *Geophysics*, **48**, 1514-1524.

Ben-Menahem, A. and Singh, S.J. [1981]. *Seismic Waves and Sources*. Springer Link.

Castagna, J.P., Batzle, M.L. and Eastwood, R.L. [1985]. Relationships between compressional-wave and shear-wave velocities in clastic silicate rocks: *Geophysics*, **50**, 571-581.

Duan, Y. and Sava, P. [2010]. *Imaging condition for elastic RTM*, CWP809 report, Center for Wave Phenomena. Colorado School of Mines.

Gardner, G.H.F. Gardner, L.W. and Gregory, A.R. [1974]. Formation velocity and density -- the diagnostic basics for stratigraphic traps. *Geophysics,* **39**, 770-780.

Gray, S., Trad, D., Biondo, B. and Larry, L. [2006]. Towards Wave-equation imaging and velocity estimation. *CSEG Recorder* vol 31.

Howard, M. [2007]. Marine seismic surveys with enhanced azimuth coverage: Lessons in survey design and acquisition: *The Leading Edge*, **26**, 480-493.

Kosloff, D., Sherwood, J., Korem, Z., Machet, E. and Falkovitz, Y. [1996]. Velocity and interface depth determination by tomography of depth migrated gathers. *Geophysics*, **61**, 1511-1523.

Langton, D., Biholar, A., Shaw, K., Adams, S., Bradshaw, M., Codd, J., Tan, X., Bartana, A. and Kessler, D. [2019]. Elastic imaging and its benefits – Permian Basin example. *First Break,* 69-77.

Jing, C., Singh, V., Custodio, D., Cha, Y. and Ross, W. [2017]. *Benefits and applications of elastic reverse time migration in salt related imaging*. SEG Annual Meeting, Expanded Abstracts.

Mifflin, C., Eddy, D., Wray, B., Zheng, L., Chazalnoel, N. and Huang, R. [2021]. Shenzi OBN: An imaging step change, *The Leading Edge*, 348-356.

Pacal, E., Stewart, R., Baysa,l E. and Yilmaz, O. [2015]. *Seismic imaging with Ocean-bottom nodes (OBN): Mirror migration technique*. SEG Annual Meeting, Expanded Abstracts.

Samec, P. and Blangy, J.P. [1992]. *Viscoelastic attenuation, anisotropy, and AVO, Geophysics*, **57**, 441-450 https://doi.org/10.1190/1.1443258.

Stork, C. [1992]. Reflection tomography for the post-migrated domain. *Geophysics*, **57**, 680-692.

Tarantola, A. [2005]. *Inverse problem theory and methods for model parameter estimation*, SIAM.

Vigh, D., Kun, Xin Cheng, J., Dong, S. and Winston, L. [2016]. Earth-model building from shallow to deep with full-waveform inversion. *The Leading Edge* 2016, **35**, 1025-1030.